Icarus 238 (2014) 77–85

Contents lists available at ScienceDirect

Icarus

journal homepage: www.elsevier.com/locate/icarus

Grid-free 2D plasma simulations of the complex interaction between the solar wind and small, near-Earth asteroids

M.I. Zimmerman [a,d,*], W.M. Farrell [b,d], A.R. Poppe [c,d]

[a] Johns Hopkins University Applied Physics Laboratory, Laurel, MD 20723, USA
[b] NASA Goddard Space Flight Center, Greenbelt, MD 20771, USA
[c] Space Sciences Laboratory, University of California, Berkeley, CA 94720, USA
[d] NASA Lunar Science Institute, Ames Research Center, Moffett Field, CA 94089, USA

ARTICLE INFO

Article history:
Received 20 September 2013
Revised 23 January 2014
Accepted 27 February 2014
Available online 4 April 2014

Keywords:
Asteroids
Solar wind

ABSTRACT

We present results from a new grid-free 2D plasma simulation code applied to a small, unmagnetized body immersed in the streaming solar wind plasma. The body was purposely modeled as an irregular shape in order to examine photoemission and solar wind plasma flow in high detail on the dayside, nightside, terminator and surface-depressed 'pocket' regions. Our objective is to examine the overall morphology of the various plasma interaction regions that form around a small body like a small near-Earth asteroid (NEA). We find that the object obstructs the solar wind flow and creates a trailing wake region downstream, which involves the interplay between surface charging and ambipolar plasma expansion. Photoemission is modeled as a steady outflow of electrons from illuminated portions of the surface, and under direct illumination the surface forms a non-monotonic or "double-sheath" electric potential upstream of the body, which is important for understanding trajectories and equilibria of lofted dust grains in the presence of a complex asteroid geometry. The largest electric fields are found at the terminators, where ambipolar plasma expansion in the body-sized nightside wake merges seamlessly with the thin photoelectric sheath on the dayside. The pocket regions are found to be especially complex, with nearby sunlit regions of positive potential electrically connected to unlit negative potentials and forming adjacent natural electric dipoles. For objects near the surface, we find electrical dissipation times (through collection of local environmental solar wind currents) that vary over at least 5 orders of magnitude: from 39 μs inside the near-surface photoelectron cloud under direct sunlight to $\gg$1 s inside the particle-depleted nightside wake and shadowed pocket regions.

1. Introduction

Airless bodies in the Solar System – from tiny dust grains to large moons – obstruct the local flow of solar wind, collect its charged particles, and create plasma wakes, generating complex and interesting electric field and potential structure. On the larger side of the spectrum is Earth's Moon, which at radius $R_M \sim 1740$ km creates a global plasma wake that typically extends tens of lunar radii downstream. The lunar dayside is dominated by photoemission, which generates a dense layer of photoelectrons within just meters above the surface (Poppe and Horányi, 2010). The lunar nightside collects the most energetic solar wind electrons penetrating the wake and can charge to thousands of Volts negative (Halekas et al., 2005). Regional irregularities in the surface topography – such as craters and outcroppings – can generate their own mini-wakes that significantly affect the local particle fluxes and electric field, most notably near the lunar terminator and poles (Farrell et al., 2010; Zimmerman et al., 2011, 2012, 2013; Poppe et al., 2012). Some of the most important factors governing the plasma–Moon interaction are the effective body size R, the typical solar wind Debye length $\lambda_{sw} \sim 10$ m, the dayside photoelectron Debye length $\lambda_{pe} \sim 1$ m, the thermal ion and electron gyroradii in the interplanetary magnetic field, $\rho_i \sim 120$ km and $\rho_e \sim 3$ km, the ion Mach angle $\theta_M = \tan^{-1}(c_s/v_{sw}) \sim 6°$, where $c_s = 4 \times 10^4$ m/s is the ion sound speed and $v_{sw} = 4 \times 10^5$ m/s is the solar wind flow speed.

Lunar-relevant processes should also be important at intermediate body sizes, such as at asteroids tens to hundreds of meters in size (or even lunar rocks, boulders, and craters at these scales). However, given the smaller spatial scale of an asteroid, namely the closer proximity of sunlit and shadowed surfaces with respect to the solar wind Debye length of about 10 m, the day and night

* Corresponding author at: Johns Hopkins University Applied Physics Laboratory, 11100 Johns Hopkins Road, Laurel, MD 20723, USA.
E-mail address: Michael.Zimmerman@jhuapl.edu (M.I. Zimmerman).

http://dx.doi.org/10.1016/j.icarus.2014.02.029
0019-1035/

processes that would seem quite distinct and separate on larger scales at the Moon may be more strongly intertwined. For instance, it is unclear how the thin dayside sheath merges with an asteroid's nightside global wake, how minor surface irregularities could modulate the formation of adjacent mini-wakes and photoemissive regions across the body, and what electric field, electric potential, and surface charging distributions exist in various unique geographic regions around the asteroid. In the present work plasma treecode simulations are used to address these issues, which will be very important to future asteroid rendezvous and retrieval missions. This new focus on the complex plasma environment of a small asteroid represents the natural evolution of long-standing computational efforts for the NASA Lunar Science Institute/Dynamic Response of the Environment At the Moon (DREAM) team to understand the airless lunar plasma and electrostatic environment. Anticipating the local ground potential and electric field environment at an asteroid will help in efforts to mitigate electrostatic charging hazards for sensitive instrumentation and electronics, especially if repeated contact is planned during a future mission.

An accurate knowledge of the electrostatic plasma environment at airless bodies, including both Earth's Moon and asteroids, is also critical for understanding the electrostatic charging and possible levitation/transport of micron and sub-micron sized dust grains. Electrostatic dust levitation has been confirmed in laboratory experiments relevant to airless Solar System environments (Sickafoose et al., 2000, 2001, 2002; Wang et al., 2009, 2010, 2011). Yet, it remains unverified *in situ* despite a small handful of evidence provided by excess brightness in Apollo-era lunar photographs (McCoy and Criswell, 1974; Glenar et al., 2011; Rennilson and Criswell, 1974) and dust detector experiments (Berg et al., 1973, 1974), as well as more recent detailed observations of dust "ponds" on Asteroid 433 Eros (Robinson et al., 2001; Veverka et al., 2001; Cheng et al., 2002). Recent numerical studies have constrained the size of levitating dust near the photoelectron-rich lunar dayside surface to no more than 0.1 μm (Poppe and Horányi, 2010), and have highlighted the important role that particle cohesion plays in preventing sub-micron grains from lifting off airless, near-Earth regoliths (Hartzell and Scheeres, 2011; Hartzell et al., 2013). However, it has long been proposed that extremely strong electric fields (>10 kV m^{-1}) arise near abrupt day/night boundaries, where neighboring sunlit (photoelectron-emitting) and shadowed (electron-collecting) patches could develop large charge differences (Criswell and De, 1977; De and Criswell, 1977; Wang et al., 2007). Such extreme electric fields would certainly be capable of supporting dust grains electrostatically; however, more recent simulations that have included the presence of the neutralizing background solar wind plasma have shown that such strong electric fields are suppressed, even with neighboring sunlit/shadowed patches (Poppe et al., 2012). Such simulations did show electric field enhancements near the terminator regions roughly three to five times the nominal dayside strength and left open the possibility of electric field enhancements of this magnitude on asteroidal surfaces with complex topographies, such as considered here.

In the present work we use a newly-developed electrostatic treecode to simulate the field and plasma environment around an asteroid tens to hundreds of meters in size. A number of plasma simulation and analytical efforts already exist in the small-asteroid size regime, primarily aimed at investigating the effects of strong intrinsic magnetization and bow shock formation on multi-km scales (Simon et al., 2006; Wang and Kivelson, 1996; Baumgartel et al., 1997). However, for the small, unmagnetized bodies of interest herein these electromagnetic complications may be neglected since $R \ll \rho_e \ll \rho_i$. In this small-body regime the particles effectively feel no appreciable magnetic force while traversing the length of the obstructing object. A more recent 2D simulation effort was carried out by Nakagawa (2013), who used a two-dimensional particle-in-cell code to study the solar wind interaction with an $R \sim 30$ m spherical asteroid that was not illuminated by the Sun (i.e., no photoemission). The present work differs significantly in that it incorporates a full photoemission model that is dependent on solar incidence angle as well as the shadowing effects of any upstream topography. With this technical advancement, as well as several other computational advantages of tree-based field solvers that will be discussed in Section 2, the treecode represents an extremely powerful physics-based tool for simulating the plasma environment of small asteroids in 2D. In two dimensions any non-trivial topographic variations in the third dimension are neglected (e.g. an object with a circular 2D cross-section effectively models an infinitely long cylinder). However, our treecode implementation provides a high-quality quantitative tool for beginning to understand the many complexities of solar wind–asteroid–photoelectron interactions at intermediate length scales. While we cannot reproduce additional topographic complexities of being in 3D, simulating the basic interesting and relevant plasma physics does not require three dimensions. It will be demonstrated that two spatial dimensions are enough to provide a clear picture of wake and photoelectron sheath formation under a wide range of local illumination and plasma flow conditions.

Poppe et al. (2012) performed 1D particle-in-cell simulations showing that modulation of the photoelectron sheath due to changing solar zenith angle can significantly affect the plasma environment of a small, 5 m-diameter lunar crater. Ergun et al. (2010) performed hybrid 3D simulations of spacecraft charging near the Sun and characterized the resulting photoelectron and wake environment. Here, in Section 3, we present basic plasma physics results for an irregularly shaped asteroid about 200 m in length and 50–100 m in width, which is much larger in scale than these previous simulations, particularly in the ratio of body size to photoelectron and solar wind Debye lengths. The primary objective will be to identify and understand key morphological plasma/surface interaction regions that form about a small asteroid body. Particular attention is paid to (1) how the transition from sunlight to shadow affects surface charging and the resulting near-surface electric field and particle flows, (2) how a mini-wake forms in a small, shadowed pocket, and (3) how all of these smaller structures merge into the larger "global" wake created downstream of the body. Other, finer details such as quantifying the shapes of particle distribution functions, wave activity, electric potential and field profiles, and magnetic field effects are deferred in favor of a broader investigation of the baseline, quasi-static plasma environment. The direct relevance of the plasma and field environment to future exploration efforts is discussed in Section 4, and concluding remarks are given in Section 5.

2. Computational methodology

Gridless treecodes were first developed to accelerate the computation of $O(N^2)$ interparticle gravitational forces in an astrodynamical context (e.g., Barnes and Hut, 1986). An excellent review of the treecode paradigm as adapted to kinetic plasma simulations – where electric rather than gravitational forces are computed – is given by Christlieb et al. (2006), and we have based our present 2D electric field and potential solvers on the formalism laid out in their paper. Our treecode essentially divides plasma simulation particles (each representing a finite group of many real particles) into small "clusters" and then efficiently calculates cluster-particle forces by way of a multipole approximation. Once the self-consistent electric field is sampled by all particles they are advanced in time via Newton's second law and accumulated on

any incident interior surfaces. Secondary and photo-emitted species are released from each part of the surface as appropriate, and the process repeats. The recursive subdivision procedure in the treecode approach is a natural choice for the present small-body simulations: it creates more and smaller clusters of particles in high-density photoelectron rich zones where the Debye length is small and high detail is needed, and less and larger groups in low-density obstructed wake regions where the Debye length is large. In effect this paradigm maximizes simplicity and robustness of the code, compared with a more traditional particle-in-cell approach, which would require a cumbersome multi-level or conformally mapped grid to apply fine resolution in high-plasma-density regions while maintaining computational efficiency.

A further technical advantage of the treecode approach is that the boundary conditions are very simple for use within the present context of open plasma flows. Rather than needing to specify unphysical distributions of charge, potential, or electric field on the simulation boundaries (which is required in PIC) we simply assume there is zero net charge outside the domain. All simulated electric fields come from particles and charged surfaces within the simulated domain. This amounts to assuming that the surrounding plasma is quasineutral (which is not a bad approximation so long as the near-surface interaction regions and trailing wake are largely contained within the simulated domain). Thus, the charge density source term in Poisson's equation is effectively zero outside the domain and no additional explicit or implicit surface-bound source terms are required at the simulation edges. Indeed, in past efforts we have encountered anomalous strong electric fields forming at the edges of traditional PIC simulations with Dirichlet or Neumann boundary conditions on the electric potential, which required some adjustment of the injected particle distributions as well as very large simulation domains to generate desired conditions well within the interior (cf. Zimmerman et al., 2011, 2012). The treecode seems to mitigate edge effects to a large degree, which is a highly desirable feature that we are continuing to investigate.

A crucial part of the simulation code is the representation of surfaces, which requires detailed models of shadowing of the Sun's incident light, photoemission, and surface charging. Each object within the domain is represented as series of connected, flat segments that can collect charge, emit photoelectrons with a cosine dependence on angle of solar incidence (if illuminated at all), and emit secondary electrons due to impacts by solar wind electrons. A simple ray-casting algorithm determines which segments are sunlit or shadowed under a user-specified solar illumination vector. The electric field due to accumulated surface charge is computed using an exact analytic expression for an infinitely deep flat plate derived from Coulomb's law in 2D planar coordinates. Carrying out this computation for each segment/particle pair incurs a moderate cost over other more approximate schemes, such as placing all the surface charge at the center point of each segment and treating it as a monopole; however employing the full analytic expression provides the very important benefit of mitigating strong fringing fields that unphysically scatter particles near joints between surface segments. Sufficiently far away from each segment a multipole approximation could be used in place of the complete Coulomb solution to potentially improve performance.

The other physically critical piece of the code is in the initial loading of particles and subsequent injection of particles at the boundaries. Solar wind particles are loaded according to a Maxwellian velocity distribution function with a flow velocity $v_d = 4 \times 10^5$ m/s along the x-direction with drift speed and with electron thermal speed $v_{the} = 2 \times 10^6$ m/s and ion sound speed $c_s = 4 \times 10^4$ m/s (10 eV plasma temperature). Particles are continuously injected into the domain from the upstream and lateral boundaries using Maxwellian flux distribution functions, and the fastest electrons can be reflected at the downstream boundary to avoid a charge buildup there (cf. Zimmerman et al., 2011). Photoelectrons are represented by a Maxwellian velocity distribution function with $v_{thpe} = 6 \times 10^5$ m/s, and a base emission current of $I_{pe} = 4$ μA under normal solar incidence (cf. Poppe and Horányi, 2010). The background solar wind density is set to a representative quiet-time value of $n_0 = 5 \times 10^6$ m^{-3}. In the present work each simulated electron and proton represents 50 million real particles of the respective species, the electron and photoelectron masses take their respective natural values of $m_e = 9.109 \times 10^{-31}$ kg and $m_p = 1.673 \times 10^{-27}$ kg, and the maximum number of particles per leaf cell was set to 20 (giving about 1.25×10^9 real or 25 simulated particles per bulk Debye square equating to about 1.25 leaf cells per Debye square). In our implementation the electric field and potential are computed exactly for particles within 2–3 neighboring cells of one another, so having approximately 1 leaf cell per Debye length does not imply an unreasonably coarse local resolution. The simulation timestep is 5×10^{-7} s, which is about 1/20 of the dayside photoelectron plasma period assuming a near-surface density on the order of 10^8 m^{-3}. Surface segments average about 10 m in length and are slightly smaller in regions of convex curvature – this size is large enough not to incur considerable additional computational cost and small enough to finely resolve variations in charging and illumination conditions along a 100–200 m-size body's surface.

A magnetic field is not included since the target object size of <200 m and, particularly, the fine topographic features <50 m in size are only a few percent of the typical plasma particle gyroradii $\rho_i \sim 120$ km and $\rho_e \sim 3$ km. A typical plasma electron would only undergo a small fraction of a gyroorbit while traversing the length of the object, and the faster tail electrons which make a more significant contribution to nightside surface charging and wake formation will have even larger gyroradii and behave even more ballistically (cf. the appendix of Zimmerman et al., 2013).

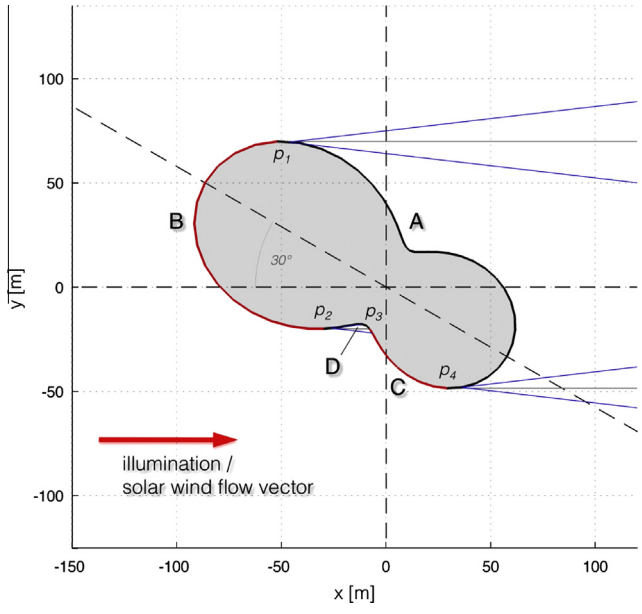

Fig. 1. Schematic representation of the simulated asteroid surface, inclined at 30° with respect to the sunward direction. There are four distinct illumination regions: (A) shadowed nightside, (B and C) illuminated dayside, and (D) shadowed pocket. Shadowed surfaces are shown in black, illuminated ones are shown in red, and there are four boundaries between light and dark, denoted by p_1–p_4; the boundary at p_3 is abrupt and the others are more gradual. The optical shadow of the body is denoted by thin gray lines, and ion mach cones are denoted by thin blue lines. (For interpretation of the references to color in this figure legend, the reader is referred to the web version of this article.)

3. Electrostatic and plasma environment of a small asteroid

The asteroid surface generated for this study is shown in Fig. 1. A smooth, double-lobed geometry is chosen to provide some complexity of shape while still revealing the governing physics in a straightforward manner. On its primary "long" axis the object is about 200 m in length, its large and small lobes are respectively about 100 m and 60 m in diameter, and the body axis makes a 30° angle with respect to the sunward vector (which points along the negative x axis in Fig. 1). At this orientation there are four distinct illumination regions along the surface, which are denoted in Fig. 1 – unlit regions are drawn in black and lit regions are drawn in red. The shadowed nightside area, or surface A, comprises the entire "back" side of the body, dayside surfaces B and C comprise the directly illuminated "front" parts of the two lobes, and a shadowed "pocket", or surface D, lies between dayside B and C. These labels will also be used to refer to the spatial regions near the respective surfaces; e.g. dayside B and C will also denote the regions just upstream of the respective illuminated parts of the large and small lobes, the pocket D will also denote the region between dayside B and C, and the nightside A will also refer to the full obstructed region downstream. There are four boundaries between sunlight and shadow, denoted as p_1–p_4 in Fig. 1. At occultation points p_1, p_2, and p_4 the solar incidence angle (and thus the emitted photoelectron flux) tapers off smoothly to zero, and at p_3 the photoemission boundary is more abruptly defined by the shadow of the larger lobe, dayside B.

Figs. 2–6 show time-averaged simulation results from the treecode, including electric field (Fig. 2), concentration and fluid velocity vectors of solar wind electrons (incl. secondary electrons, Fig. 3), solar wind protons (Fig. 4), and emitted photoelectrons (Fig. 5), as well as electric potential (Fig. 6). The total simulation domain for these figures was 0–3 km in the horizontal x-direction and −750 m to 750 m in the vertical y-direction, and time-averaging was carried out using 100 instantaneous snapshots taken at intervals of 500 timesteps after the simulation reached a quasisteady equilibrium. Pointing to Figs. 2–5 we will discuss the various physical processes involved in generating the very distinct nightside and dayside regions, and we will then discuss the complex transition areas in between (near the terminator points p_1 and p_4), as well as the pocket region which combines elements of day and night in a very interesting and physically significant manner. Finally, the electric potential of Fig. 6 will be examined within the context of these other findings.

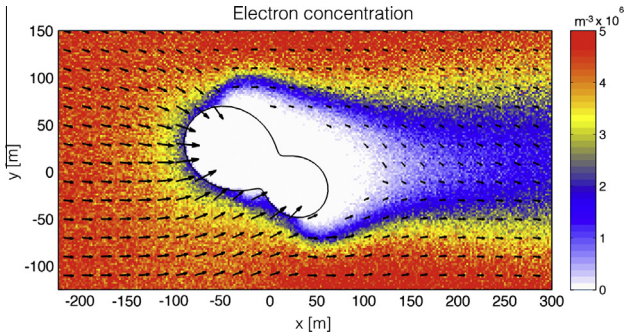

Fig. 3. Time-averaged solar wind electron concentration and velocity vectors for the asteroid of Fig. 1.

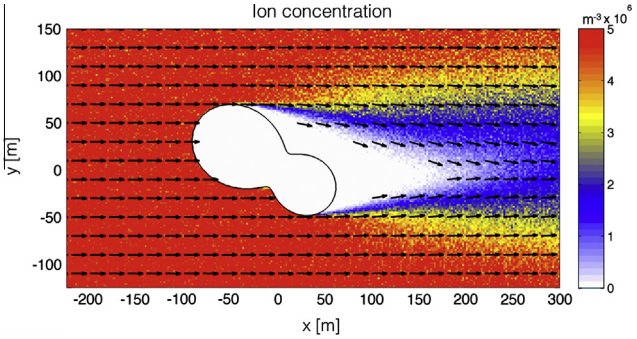

Fig. 4. Time-averaged solar wind proton concentration and velocity vectors for the asteroid of Fig. 1.

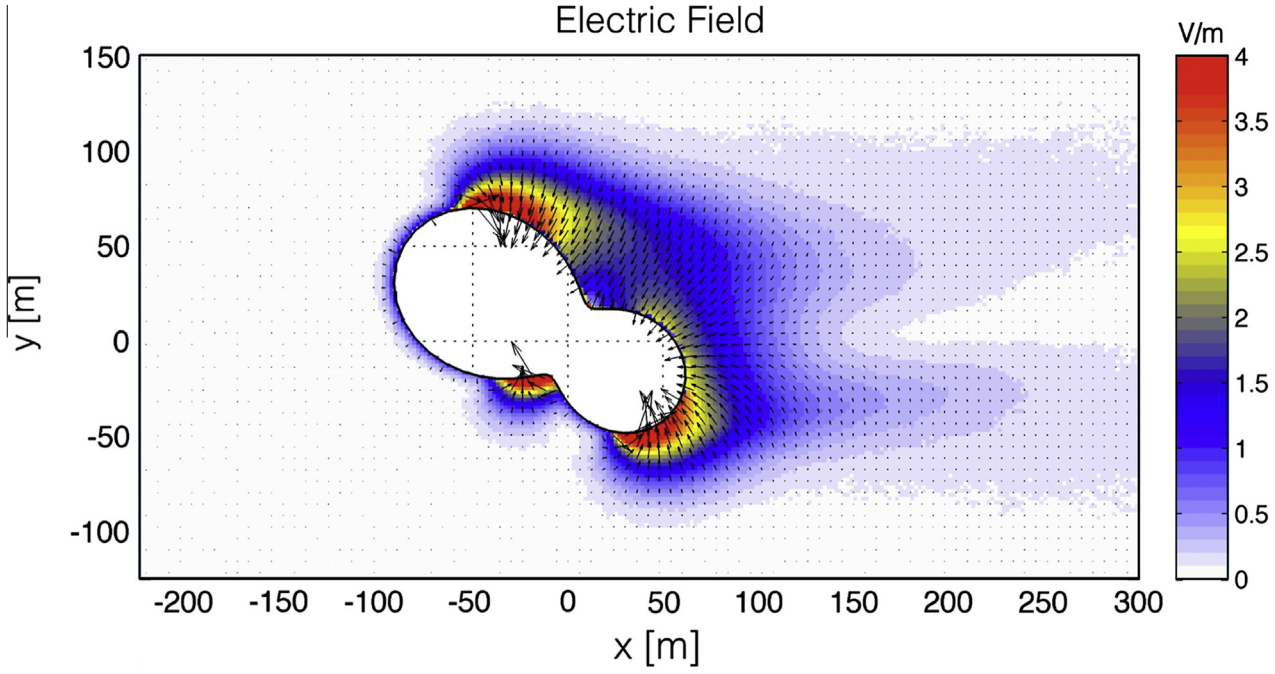

Fig. 2. Time-averaged electric field vectors and magnitude produced by the simulated interaction of the solar wind with the asteroid surface of Fig. 1. The electric field magnitude reaches 9 V/m in the red saturated regions near the terminators p_1 and p_4, and 6 V/m in the pocket near p_2 and p_3.

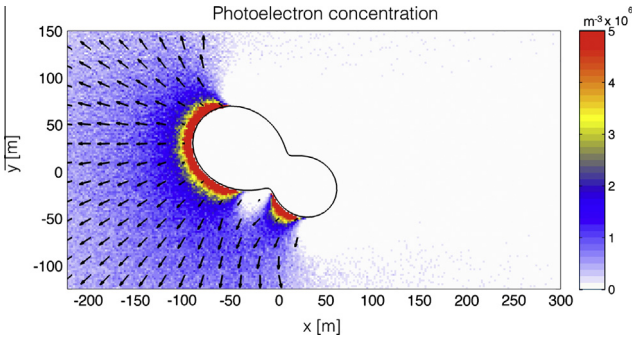

Fig. 5. Time-averaged, emitted photoelectron concentration and velocity vectors for the asteroid of Fig. 1.

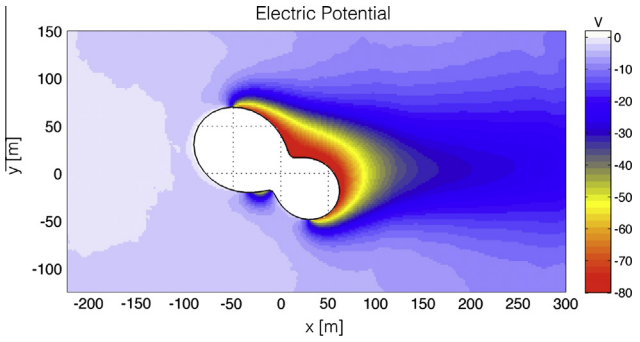

Fig. 6. Time-averaged electric potential structure produced by the interaction between the flowing solar wind and the asteroid surface of Fig. 1.

3.1. Nightside (region A)

The nightside surface collects solar wind electrons and emits secondary electrons, forming a large inward electric field and establishing current balance, or net zero current to the surface. This surface-charge electric field is shown in Fig. 2 and has very strong (red saturated) signatures of up to 9 V/m near the shadowed boundaries of the nightside (at points p_1 and p_4) and a weaker but still significant (blue) signature of 1–1.5 V/m extending downstream to about $x = 125$ m. The electron concentration patterns of Fig. 3 show that the surface-charge field component creates plasma sheaths forcing electrons away from the surface near p_1, p_4, and the deepest parts of the nightside. Farther downstream the electric field transitions from being surface-charge dominated to ambipolar-dominated where the simulation results are well aligned with theory. For instance, beyond about $x = 125$ m downstream – where the nightside surface charge effects begin to taper off – comparison of electron and ion concentrations in Figs. 3 and 4 show that electrons rush into the nightside region ahead of the protons, creating a more traditional ambipolar wake structure (cf. Samir et al., 1983). In the electric field of Fig. 2, ambipolar wake flanks with inward-directed peak fields of about 1.5 V/m extend down the entire length of the simulation. Fig. 4 shows that solar wind ions that would otherwise thermally diffuse into the wake region at about the Mach angle of $\tan^{-1}(c_s/v_{sw}) \sim 6°$ (shown in Fig. 1 as thin blue dashed lines) actually accelerate into the void at larger angles because of the ambipolar field generated along the flanks. In addition, an ion rarefaction wave propagates outward from the body at roughly the Mach angle, as evidenced by the extended yellow colored region of the ion concentration in Fig. 4. These regions of lower ion density radiate out into the solar wind roughly from the occultation points p_1 and p_4 consistent with a self-similar ion sonic wake as predicted by theory (cf. Crow et al., 1975; Mora and Pellat, 1979; Samir et al., 1983).

3.2. Dayside (regions B and C)

On the sunlit side of the asteroid the basic kinetics are quite different than on the nightside. Here, the electric field and plasma environment are photoemission dominated, since the emitted photoelectron flux $F_{pe} = I_{pe}/e \sim 2.8 \times 10^{13}$ m^{-2} s^{-1}, where $I_{pe} = 4.5$ μA m^{-2} and $e = 1.6 \times 10^{-19}$ C, is about 3–10 times higher than the solar wind electron and ion fluxes $F_e = n_e v_{the} = 1 \times 10^{13}$ m^{-2} s^{-1} and $F_i = n_i v_{sw} = 2 \times 10^{12}$ m^{-2} s^{-1}. The photoelectron concentration of Fig. 5 in comparison with the electron and proton concentrations of Figs. 3 and 4 further illuminates this point. We note that different velocities are used in the solar wind flux calculations because (1) the electron thermal speed is much larger than the plasma drift speed and represents by far the most significant contribution to the electron flux and (2) the drift speed is much larger than the ion sound speed and thus characterizes the beam-like flux of protons. Near the dayside surfaces B and C the photoelectron number density approaches $\sim 10^8$ m^{-3} (within the saturated red regions of Fig. 5, which only shows isocontours up to the nominal solar wind density of 5×10^6 m^{-3}) which is two orders of magnitude greater than the background solar wind concentrations of 10^6 m^{-3}. Fig. 2 also shows outward directed electric field vectors of about 1.5 V/m in magnitude near dayside B and C, which serve to recapture many of the emitted photoelectrons. This explains the near-zero photoelectron velocity vectors in the deep red, high-concentration areas of Fig. 5. In these regions slightly more than half the photoelectron population is moving away from the surface and almost half turns around within the first 10–15 m above the surface, which causes a significant buildup of negative photoelectric charge near the surface. There is also a null in the electric field just above the directly illuminated surfaces where the inward electric field created by the photoelectron sheath balances the outward surface electric field that forms due to a net positive surface charge. These results are consistent with previous theory (Nitter et al., 1998) and simulations (Poppe and Horányi, 2010; Farrell et al., 2013). From the electron velocity vectors of Fig. 3 it is clear that solar wind electrons experience a net flow into the photoelectron sheaths, largely because the body itself has blocked the outward-moving portion of the electron distribution leaving only the inward-moving half traveling toward the local surface. Comparing the photoelectron concentration of Fig. 5 with the solar wind electron concentration of Fig. 3 suggests that the photoelectrons actually displace some solar wind electrons (in dayside regions where the concentration is colored yellow in Fig. 3). This photoelectron outflow is part of a precursor effect (Halekas et al., 2012) wherein the solar wind begins to "sense" the object via the electric field created by its dayside photoelectron population from hundreds of meters upstream. The precursor effect is also noticeable in the very slightly positive dayside electric potential between $x \sim -100$ m to -50 m in Fig. 6, which is due to the net negative space charge created by the photoelectron stream emitting from the illuminated larger lobe.

3.3. Terminators (points p_1 and p_4)

The terminating boundaries between sunlight and shadow generate complicated and interesting field structure. Close inspection of the terminator points p_1 and p_4 reveals a dipolar field structure in Fig. 2, with the outward-pointing electric field on the illuminated side curving around to meet the stronger inward-pointing electric field in shadow. This represents the merger between the relatively thin but dense photoelectron sheath on the illuminated side and the thicker but more tenuous solar wind plasma sheath just behind the local terminator. At both p_1 and p_4 the dipolar field is centered in the region where photoemission begins to fall off sharply, a few degrees to the sunward side of the actual local terminator, which

is qualitatively consistent with the analytical current-balance predictions of Farrell et al. (2007). This electric field repels photoelectrons toward the dayside (see Fig. 5), demonstrating the high effective conductivity of the dayside photoelectron sheath, as been noted for the Moon (Wang et al., 2007; Farrell et al., 2013; De and Criswell, 1977; Criswell and De, 1977). Given sufficient near surface concentration a few degrees off the local terminator, photoelectrons are able to quickly respond to and short out any externally imposed electric fields. This is consistent with the meter-scale lunar crater simulations of Poppe et al. (2012), who found that the presence of photoemission significantly modifies the small-crater plasma environment as the solar zenith angle changes.

In addition to the dipole structural nature of the E-field at the terminator locations (p_1 and p_4), the field also has its largest values in these regions, saturating at about 9 V/m. At the terminator and into the nightside regions, the surface potential is negative (Fig. 6) and an electric-field then develops to retard/reject the electrons from the near-surface region; this effect is evident in Fig. 3, where the regions of lower electron density near the terminators (white regions) are noticeable at p_1 and p_4. In essence, the near-surface Debye sheath potential creates an electron repulsion zone that extends a few Debye lengths downstream of the object. However, farther downstream away from the negatively-charged nightside surface, the electrons penetrate into the wake ahead of the solar wind ion flow, driving the ambipolar expansion process. Comparing Figs. 3 and 4 in the near terminator and downstream regions, it becomes evident that the negative surface "stands off" the flow of electrons, leaving an ion-rich interaction region with $n_i > n_e$ within a few Debye lengths above the terminators. This can be seen most clearly by comparing the approximate flow of ions given by the ion mach cone in Fig. 1 or the exact ion flow of Fig. 4 with the near-terminator depletion in electron density above the terminators in Fig. 3. Farther downstream of the terminators the electrons begin to rush into the core of the wake, forming a negative electron cloud with $n_e > n_i$.

3.4. Pocket (region D, points p_2 and p_3)

The pocket region of Fig. 1 defines a uniquely shadowed topographic area lying between the two dayside illuminated regions. This area is about 5 m deep, which is small compared with the overall 100-m asteroid; however, it creates one of the most significant electric field regions in the entire domain. Fig. 2 shows an inward electric field of greater than 3.5 V/m, up to 6 V/m, in the vicinity of the pocket, which being adjacent to the weaker outward field vectors of the dayside areas forms dipolar field structures near the edges of the pocket at points p_2 and p_3. As with the near-terminator regions of daysides B and C (i.e. around p_1 and p_4), the electron and photoelectron concentrations and velocities shown in Figs. 3 and 5 indicate that most of the thermal, low-energy electrons are rejected from the pocket by the strong, inward-pointing electric field.

By analogy, other shadowed pockets near the terminator should have similar structure, and for a surface that is littered with pockets or craters, we can anticipate a surface E-field structure that is highly variable in both magnitude and orientation due to locations being in and out of shadow.

3.5. Overall potential structure

Fig. 6 shows the simulated electric potential generated by the asteroid/solar wind interaction. The largest and most obvious potential drop is about −80 V (with respect to the bulk solar wind far upstream of the object) and is associated with the wake formation process occurring on the nightside of the asteroid. Especially near the nightside surface the particle density is low and dominated by the energetic tail of the solar wind electron distribution, i.e. those electrons with enough energy to propagate through both the ambipolar and surface potential drops. The potential that develops trailing the object is significant. The equipotential lines radiate outward from the main terminators at p_1 and p_4 where the rapid change from a high to low surface potential is governed by the transition from positive surface charging in sunlight to negative surface charging in shadow. Solar wind electrons govern the locally vertical potential structure near each terminator as they quickly respond to the negative surface charge on the nearby body.

We note that the trailing wake related potential structure has two distinct regions in Fig. 6. There is a Debye sheath (red region with sharp yellow boundary) associated with the negative surface charge and an extended ambipolar expansion region (in blue for $x > 100$-m). For the nightside Debye sheath, the potential gradient layer is roughly a few local Debye lengths thick, and $n_e > n_i$. Beyond about 100-m downstream, the potential becomes dominated by ambipolar wake expansion processes (Samir et al., 1983), and electrons propagate inward to the central wake region ahead of the ions. This electron 'cloud' region (Crow et al., 1975) where $n_e > n_i$, is evident in a comparison of Figs. 3 and 2 between $100 < x < 200$ and $-50 < y < 50$.

The pocket region also contains a noticeable potential drop of about −40 V associated with the strong electric field seen within the pocket in Fig. 2. The local maximum in potential is not observed directly on the pocket floor, but along the leeward edge of the pocket, just adjacent to point p_2. At these locations, the plasma electrons and ions have different flow patterns, and the potentials develop to ensure equal electron and ion flux to the local surface.

Along the sunlit dayside surface, a thin photoelectron layer a few m thick forms. The potential in this region is 0–4 V positive and decreases in magnitude with solar incidence angle. Close inspection of the vertical structure near the locally subsolar dayside region also reveals a non-monotonic, or "double-sheath" potential, which represents the precursor interaction of the solar wind with the surface (Poppe and Horányi, 2010). Specifically, in these regions the ~4 V positive surface potential decreases rapidly in the first few meters above the surface but then maintains a slightly negative value out to about 100 m from the surface where it eventually returns close to 0 V. This type of potential structure has been predicted for the dayside of the Moon (Nitter et al., 1998; Poppe and Horányi, 2010), where the electric field contributions of the thin photoelectron sheath and larger-scale solar wind plasma sheath compete to form a small "double-sheath" potential well in the first hundred or so meters above the surface.

We note also that the present simulations confirm the presence near the terminators of the continuous two-dimensional merger between illuminated double-sheath regions and directly adjacent shadowed regions that exist near p_1 and p_4. At the 10–100 m scale sizes modeled herein the effects of wake formation begin to dominate over photoemission a few degrees forward of the physical terminator. This effect is seen in Fig. 3's solar wind electron concentration where the region of electron rejection from the surface extends slightly across terminator points p_1 and p_4. As such, our simulation model is able to properly include the creation of horizontal E-fields that connect nightside and dayside regions, and which allow an encroachment of one region into the other. Merging between the dayside photoelectron sheath and trailing wake was also observed in the meter-scale simulations of Ergun et al. (2010), who saw photoelectrons escaping on the illuminated side of a spacecraft near the Sun and wake formation with an associated negative electric potential on the shadowed side.

4. Discussion

Table 1 shows key physical values for regions and points on the surface. In general, the dayside regions are dominated by positive

Table 1
Summary of plasma properties near the asteroid surface in Fig. 1. Dissipation times were calculated using Eq. (2) of Farrell et al. (2008), which is $\tau \sim (\sqrt{\pi} C m_e V_{th}^2)/(e^2 n v_{th} A)$ where $C \sim 100$ pF is the object capacitance, m_e is the electron mass, v_{th} is the local thermal speed of the dominant electron population ($v_{the} = 2 \times 10^6$ m/s, $v_{thp} = 6.2 \times 10^5$ m/s), e is the electron charge in Coulombs, n is the local electron density in m^{-3}, and A is the area of the charging object, in m^2, immersed in the local plasma conditions.

Spatial region	Sunlit	Surface potential (V)	Surface electric field magnitude (V/m)	Near-surface electron density (m^{-3})	Near-surface ion density (m^{-3})	Near-surface photoelectron density (m^{-3})	1 m^2-object dissipation time (s)
Nightside (A)	N	>−85 [a]	3–9	>1×10^4 [d]	>2×10^3 [d]	0	>1.3
Dayside (B)[c]	Y	0–2	2	2×10^6	5×10^6	1×10^8	3.9×10^{-5}
Dayside (C)[c]	Y	0–2 [b]	2	2×10^6	5×10^6	1×10^8	3.9×10^{-5}
Pocket (D)	N	>−60 [a]	3–6	>1×10^5 [d]	>3×10^5 [d]	0	>0.12

[a] Magnitude limited from above by maximum resolvable electron thermal speed.
[b] Relative to nearby ambient values.
[c] In central dayside region.
[d] Limited from below by macroparticle approximation.

surface charge and a dense, negative photoelectron layer above the surface. The shadowed pocket and nightside regions are dominated by negative surface charging and electron inflow, and farther downstream the nightside is dominated by plasma expansion in the wake. The dayside potential is 0–4 V positive depending on the local level of solar illumination, and we observe a non-monotonic, double-sheath precursor region within the first 100–150 m above each illuminated surface. Surface charging is intensely negative in all of the shadowed regions of the asteroid, where the surface potential can reach −80 V with respect to the bulk solar wind.

In reality, the electric potential in the shadowed regions could be more negative, since the present simulations can only resolve out to about 3–4 thermal speeds on the tail of the Maxwellian electron velocity distribution function (vdf). At this limiting electron energy secondary emission is still relatively weak and unable to provide full current balance. This issue was noted in Zimmerman et al. (2011) and is due to the macroparticle approximation employed. The situation could be improved by representing less real particles per macroparticle – thereby increasing the number of resolved macroparticles at a significant computational cost. Also, the measured solar wind electron vdf from Lunar Prospector is more accurately described as a kappa distribution than a Maxwellian (Halekas et al., 2005). This difference could be of importance because the kappa distribution exhibits increasing temperature with increasing energy along the tails of the vdf, which actually increases secondary emission and reduces the magnitude of the electric potential on surfaces deep within the global wake (Halekas et al., 2005). The additional incoming electron flux from the tail of a kappa distribution would compete with increased loss due to secondary emission to create scientifically interesting but potentially strong and hazardous electric fields near the object.

The strongest electric field magnitude of about 6–9 V/m was found in each shadowed region, particularly near illumination/shadow boundaries p_1–p_4 where complex dipolar field structure is seen. In fact, the red-colored areas in Fig. 2 represent high-field regions where electrostatic discharging hazards could be significant for future exploration. For instance, it has been suggested that topographic irregularities on even smaller scales than those modeled herein could generate large electric fields in a process called "supercharging" (Criswell and De, 1977; De and Criswell, 1977; Wang et al., 2007). Consider the possibility of a small outward topographic bump of about 2–3 m in radius at the occultation point p_1 in Fig. 1. One side of the bump would be sunlit and would float via photoemission to a few V positive but the other side would generate a small wake and charge to 40–80 V negative under bombardment by solar wind electrons. Thus, a significant potential gradient could arise between the two sides of the bump with a maximum electric field on the order of 25 V/m, which is consistent with the meter-scale simulations of Poppe et al. (2012). The resulting dipole would also extend out into the solar wind and become shielded by plasma Debye effects starting about 10–20 m off the surface. Following this same argument, smaller irregularities could generate even stronger localized electric fields at lit/unlit boundaries under the same potential difference. Recent laboratory experiments seem to support this extrapolation (Wang et al., 2007), where kV/m electric fields were inferred between the edges of closely-placed but isolated conductors under the influence of non-uniform induced photoemission. Thus, an asteroid such as the one modeled herein likely has a fractal-like dipolar electric field structure near lit/unlit boundaries, starting at the upper scale imposed by the solar wind Debye length and moving down in size to the smallest irregularities.

Besides forming regions of supercharging, object-discharging hazards will occur in regions where the plasma content (and especially ion density) becomes small. Table 1 shows the charging dissipation times (using Eq. (2) from Farrell et al. (2008)) for an object that has collected negative tribocharge by contact with the surface regolith. The longest dissipation times (charge retention time) occur in the shadowed nightside and pocket regions where solar wind electrons and photoelectrons are electrostatically blocked from entering. In these regions, an exploration system roving on

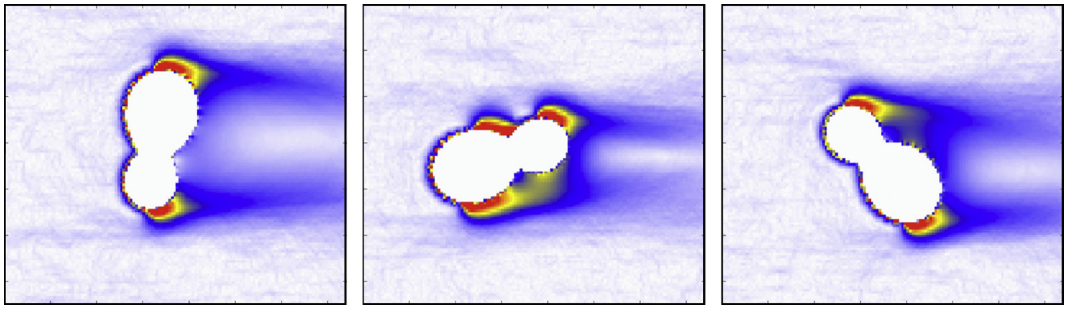

Fig. 7. Simulated electric field for three different orientations of the model asteroid, with the same color map as Fig. 2 but here the deepest shades of red correspond to an electric field magnitude of 6–9 V/m.

the surface will collect charge via tribocharging, but not easily dissipate this charge back into the weakly grounding plasma environment. In essence, in these regions, the human or robotic exploration system looses electrical contact with the plasma environment that would otherwise provide a charge reservoir and remediate the buildup of surface tribocharge. For a mission like OSIRIS-REx that will have a sample system making contact with the surface, we suggest these contacts be made in well-illuminated regions where the photoelectric sheath provides a large concentration of ambient electrons that will offset any tribo-charge buildup between the sample collector and the surface.

Of course, the rotational configuration of Figs. 1–6 represent only one orientation of the body with respect to the flow of solar wind. In a more realistic scenario the body would also tumble as it orbits through interplanetary space, effectively modulating over time which regions are shadowed and which are sunlit. Additional simulations were performed at a range of orientations from 0° to 360° in increments of 7.5°, and a few representative electric field plots are shown in Fig. 7. Additionally, the full animated figure showing electric field magnitude is downloadable as Supplementary online material. In this animation sequence the occultation points for the global wake (p_1 and p_4) as well as the associated ambipolar and surface electric fields shift dynamically around the body as it tumbles, and mini-wakes arise in pockets of temporary shadow (as shown in Fig. 7b). The photoelectron layer shifts accordingly, following the regions of direct illumination. Just as in Fig. 2, dipolar electric field structures arise between adjacent sunlit and shadowed regions. Examining the surface charging history at various orientations has suggested that the asteroid charge-equilibration timescale is a few thousand solar wind plasma periods – on the order of a few ms – and this implies that under typical solar wind conditions the surface will re-equilibrate virtually instantaneously as the asteroid rotates on a timescale of seconds or more.

5. Summary

The plasma and electrostatic environment of a small, irregularly shaped asteroid has been simulated using a newly developed tree-code. The code incorporates a full surface-charging model including the critical effects of photoemission, which is dependent on the local angle of solar incidence as well as shadowing by topography. This type of code uses a recursive adaptive refinement scheme that is computationally well suited to the disparate particle concentrations within the sunlit and shadowed regions.

In this paper, our objective was to show the overall complex morphological structures and distinct environmental regions that develop in the course of the solar wind/asteroid interaction. These regions are shown in Fig. 1 and the nominal surface plasma values for each region are outlined in Table 1. This paper is purposely intended to be a "big picture" view, and future analysis will delve into the extraordinarily rich details that occur within each region and at the terminating points p_1–p_4. These future regional focus efforts will include details on the wave–particle interactions, detailed comparisons to previous 1D work and lunar observations, and more examination on the nature of the horizontal interactions near terminating points, including horizontal forming E-fields and dust charging and dynamics. Obviously these subjects are of great interest but inclusion herein would make this presentation of the large scale structures that develop near a complex small body less deliberate.

Acknowledgments

This research was supported by an appointment to the NASA Postdoctoral Program at the Goddard Space Flight Center, administered by Oak Ridge Associated Universities through a contract with NASA. Support by the NASA Lunar Science Institute and DREAM Virtual Institute through Grant NNX09AG78A are gratefully acknowledged. M. Zimmerman thanks W. Farrell and T. Stubbs at NASA/GSFC for providing additional computing resources.

Appendix A. Supplementary data

Supplementary data associated with this article can be found, in the online version, at http://dx.doi.org/10.1016/j.icarus.2014.02.029.

References

Barnes, J., Hut, P., 1986. A hierarchical O(N log N) force-calculation algorithm. Nature 324, 446–449.
Baumgartel, K., Sauer, K., Story, T.R., 1997. Solar wind response to a magnetized asteroid: Linear theory. Icarus 129, 94–105.
Berg, O.E. et al., 1973. Apollo 17 Preliminary Science Report. Tech. Rep. NASA SP-300, pp. 16–21.
Berg, O.E., Richardson, F.F., Rhee, J.W., Auer, S., 1974. Preliminary results of a cosmic dust experiment on the Moon. Geophys. Res. Lett. 1 (7), 289–290.
Cheng, A.F., Izenberg, N., Chapman, C.R., Zuber, M.T., 2002. Ponded deposits on Asteroid 433 Eros. Meteorit. Planet. Sci. 37, 1095–1105.
Christlieb, A.J., Krasny, R., Verboncoeur, J.P., Emhoff, J.W., Boyd, I.D., 2006. Grid-free plasma simulation techniques. IEEE Trans. Plasma Sci. 34, 149–165.
Criswell, D.R., De, B.R., 1977. Intense localized photoelectric charging in the lunar sunset terminator region: 2. Supercharging at the progression of sunset. J. Geophys. Res. 82 (7), 1005–1007.
Crow, J.E., Auer, P.L., Allen, J.E., 1975. The expansion of a plasma into a vacuum. J. Plasma Phys. 14, 65–76.
De, B.R., Criswell, D.R., 1977. Intense localized photoelectric charging in the lunar sunset terminator region: 1. Development of potentials and fields. J. Geophys. Res. 82 (7), 1005–1007.
Ergun, R.E. et al., 2010. Spacecraft charging and ion wake formation in the near-Sun environment. Phys. Plasmas 17, 072903.
Farrell, W.M., Stubbs, T.J., Vondrak, R.R., Delory, G.T., Halekas, J.S., 2007. Complex electric fields near the lunar terminator: The near-surface wake and accelerated dust. Geophys. Res. Lett. 34, L14201.
Farrell, W.M. et al., 2008. Concerning the dissipation of electrically charged objects in the shadowed lunar polar regions. Geophys. Res. Lett. 35, L19104.
Farrell, W.M. et al., 2010. Anticipated electrical environment within permanently shadowed craters. J. Geophys. Res. 14 (E03004).
Farrell, W.M., Poppe, A.R., Zimmerman, M.I., Halekas, J.S., Delory, G.T., Killen, R.M., 2013. The lunar photoelectron sheath: A change in trapping efficiency during a solar storm. J. Geophys. Res. Planets 118, 1114–1122. http://dx.doi.org/10.1002/jgre.20086.
Glenar, D.A., Stubbs, T.J., McCoy, J.E., Vondrak, R.R., 2011. A reanalysis of the Apollo light scattering observations, and implications for lunar exospheric dust. Planet. Space Sci. 59, 1695–1707.
Halekas, J.S., Lin, R.P., Mitchell, D.L., 2005. Large negative lunar surface potentials in sunlight and shadow. Geophys. Res. Lett. 32, L09102. http://dx.doi.org/10.1029/2005GL022627.
Halekas et al., 2012. Lunar precursor effects in the solar wind and terrestrial magnetosphere. J. Geophys. Res. 117, A05101.
Hartzell, C.M., Scheeres, D.J., 2011. The role of cohesive forces in particle launching on the Moon and asteroids. Planet. Space Sci. 59 (14), 1758–1768.
Hartzell, C.M., Wang, X., Scheeres, D.J., Horányi, M., 2013. Experimental demonstration of the role of cohesion in electrostatic dust lofting. Geophys. Res. Lett. 40, 1038–1042.
McCoy, J.E., Criswell, D.R., 1974. Evidence for a high altitude distribution of lunar dust. Proc. Lunar Sci. Conf. 5, 2991–3005.
Mora, P., Pellat, R., 1979. Self-similar expansion of a plasma into a vacuum. Phys. Fluids 22, 2300–2304.
Nakagawa, T., 2013. Ion entry into the wake behind a non-magnetized obstacle in the solar wind: Two-dimensional particle-in-cell simulations. J. Geophys. Res. 118, 1849–1860.
Nitter, T., Havnes, O., Melandsø, F., 1998. Levitation and dynamics of charged dust in the photoelectron sheath above surfaces in space. J. Geophys. Res. 103 (A4), 6605–6620. http://dx.doi.org/10.1029/97JA03523.
Poppe, A., Horányi, M., 2010. Simulations of the photoelectron sheath and dust levitation on the lunar surface. J. Geophys. Res. 115 (A08106).
Poppe, A.R., Piquette, M., Likhanskii, A., Horányi, M., 2012. The effect of surface topography on the lunar photoelectron sheath and electrostatic dust transport. Icarus 221, 135–146.
Rennilson, J.J., Criswell, D.R., 1974. Surveyor observations of lunar horizon-glow. The Moon 10, 121–142.
Robinson, M.S., Thomas, P.C., Veverka, J., Murchie, S., Carcich, B., 2001. The nature of ponded deposits on Eros. Nature 413, 396–400.
Samir, U., Wright Jr., K.H., Stone, N.H., 1983. The expansion of plasma into a vacuum: Basic phenomena and processes and applications to space plasma physics. Rev. Geophys. Space Phys. 21, 1631–1646.

Sickafoose, A.A., Colwell, J.E., Horányi, M., Robertson, S., 2000. Photoelectric charging of dust particles in vacuum. Phys. Rev. Lett. 84 (26), 6034–6037.
Sickafoose, A.A., Colwell, J.E., Horányi, M., Robertson, S., 2001. Experimental investigations of photoelectric and triboelectric charging of dust. J. Geophys. Res. 106 (A5), 8343–8356.
Sickafoose, A.A., Colwell, J.E., Horányi, M., Robertson, S., 2002. Experimental levitation of dust grains in a plasma sheath. J. Geophys. Res. 107 (A11), 1–11.
Simon, S., Bagdonat, T., Motschmann, U., Glassmeier, K.-H., 2006. Plasma environment of magnetized asteroids: A 3-D hybrid simulation study. Ann. Geophys. 24, 407–414.
Veverka, J. et al., 2001. Imaging of small-scale features on 433 Eros from NEAR: Evidence for a complex regolith. Science 292, 484–488.
Wang, Z., Kivelson, M.G., 1996. Asteroid interaction with solar wind. J. Geophys. Res. 101, 24479–24493.
Wang, X., Horányi, M., Sternovsky, Z., Robertson, S., Morfill, G.E., 2007. A laboratory model of the lunar surface potential near boundaries between sunlit and shadowed regions. Geophys. Res. Lett. 35 (L16104).
Wang, X., Horányi, M., Robertson, S., 2009. Experiments on dust transport in plasma to investigate the origin of the lunar horizon glow. J. Geophys. Res. 114, A05103.
Wang, X., Horányi, M., Robertson, S., 2010. Investigation of dust transport on the lunar surface in a laboratory plasma with an electron beam. J. Geophys. Res. 115 (A11102).
Wang, X., Horányi, M., Robertson, S., 2011. Dust transport near electron beam impact and shadow boundaries. Planet. Space Sci. 59, 1791–1794.
Zimmerman, M.I., Farrell, W.M., Stubbs, T.J., Halekas, J.S., Jackson, T.L., 2011. Solar wind access to lunar polar craters: Feedback between surface charging and plasma expansion. Geophys. Res. Lett. 38, L19202.
Zimmerman, M.I., Jackson, T.L., Farrell, W.M., Stubbs, T.J., 2012. Plasma wake simulations and object charging in a shadowed lunar crater during a solar storm. J. Geophys. Res. 117 (E00K03).
Zimmerman, M.I., Farrell, W.M., Stubbs, T.J., 2013. Recursive plasma wake formation on the Moon and its effect on polar volatiles. Icarus 226, 992–998.